Transonic Flutter Suppression Using Active Acoustic Excitations

Pong-Jeu Lu,* Dartzi Pan,† and Dun-Yann Yeh‡
National Cheng Kung University, Tainan, Taiwan 70101, Republic of China

The objective of this work is to study the feasibility of using acoustic waves as a means for suppressing the flutter instability of a typical section in transonic flow. A high-resolution upwind TVD flow solver of acoustic accuracy was first constructed and validated on a dynamic mesh system. The geometric conservation law was implemented consistently with the physical conservation law via a suitably defined cell boundary speed. This specially developed structure/fluid/acoustic solver was then integrated in the time domain to study whether flutter can be suppressed using active acoustic excitations. Flutter suppression was achieved in the transonic region when an appropriate feedback control law was used. Large-amplitude limit cycle type oscillation in a transonic flow was also simulated. It was found that the present acoustic control technique can only be effective when the amplitude of the oscillation is small in accordance with previous findings obtained in a low-speed wind-tunnel test.

I. Introduction

A CTIVE acoustic excitation, known as one of the classical flow control techniques in aerodynamics, continues to be an important subject area that attracts much attention nowadays. Acoustic flow control has been applied successfully ranging from noise suppression,[1,2] separated-flow control,[3,4] mixing enhancement,[5] and combustion instability[6] to practical engine problems, such as surge[7] and rotating stall and buzz.[8] The recent extension to flutter suppression, which is also the concern of the present research, was first experimentally achieved by Huang.[9] Subsequently, Lu and Huang[10] performed a theoretical analysis that pointed out the basic flaws contained in Huang's explanation of the acoustic flutter suppression mechanism. The phenomenon termed trailing-edge receptivity, rather than the originally proposed hydraulic analogy, was shown analytically to be the mechanism responsible for the generation of the control forces that are required for suppressing the flutter instabilities.

In Ref. 11, problems associated with the acoustically excited transonic flowfield were investigated using a high-resolution upwind total variation diminishing (TVD) scheme. It was found that the satisfaction of the Kutta condition at the sharp trailing edge plays a central role in the acoustic/vortical wave conversion process, which, as explained by Kelvin's theorem, gives rise to the unsteady airloads produced acoustically around the airfoil. Acoustic excitation was shown to be as effective as the solid surface oscillation in producing the various types of shock motions and the unsteady airloads. The results show that, although the acoustic wave is a weak flow perturbation, the induced aerodynamic loads can be large enough to be employed as effective control forces in a transonic flow. The present work is a sequel to the previous incompressible flow investigation.[10] The main interest lies in exploring the possibility of whether this new flutter suppression technique is also applicable to transonic flow where the lowest flutter boundary is usually encountered.

Transonic flutter has been known to be closely related to the shock motions.[12,13] If the shock strength is weak, which is often the case in transonic flow, inviscid modeling can still yield reasonably good predictions of the shock waves. Since the wave interactions in a fluid are phenomena governed mainly by the convection terms of the Navier-Stokes equations, the shock and acoustic wave interaction problem can be described, at least qualitatively, with an inviscid flow

model. Therefore, in the present preliminary study, Euler equations and the Osher–Chakravarthy MUSCL type high-resolution upwind TVD scheme[14] are used as the model equations and the analysis tool, respectively.

In Ref. 15, a high-resolution scheme of acoustic accuracy was constructed by modifying the Osher–Chakravarthy scheme, which includes the nonreflective boundary condition treatment, the acoustic source modeling, and the improvements made on the interpolation of the characteristic variables over the two sides of the cell interface. This improved reconstruction of the interface variables can make the original upwind flow solver[14] more transparent to waves as they travel through a nonuniform mesh system, due to the reduction of the reflective noises among the unevenly spaced meshes.

The numerical procedure of a coupled structure/fluid time integrator is presented first, in which the structural linearity is fully utilized and the geometric conservation law is strictly implemented on the dynamic mesh system. This aeroelastic code is first validated by comparing the results with the available open-loop flutter tests. The closed-loop simulation, augmented by an active acoustic excitation and feedback control law, is conducted, and the results are compared with those obtained in the incompressible flow using V-g and root-locus methods.[10] Then the transonic flutter suppression is performed, with emphasis placed on examining the effects of forcing position and the feedback phase of the control gain. Finally, an illustrative example, attempting to show the possibility of acoustically suppressing a large-amplitude limit cycle oscillation, is simulated to shed light on the limitation of the present acoustic flutter suppression technique.

II. Numerical Methods

Aerodynamic Flow Solver

In the previous work,[15] the construction of a numerical aeroacoustic flow solver was described. Emphasis was placed upon the reduction of the numerical dissipation and dispersion effects, as well as the treatment of the boundary conditions. This time-accurate aeroacoustic solver was constructed on a stationary grid to study the intricate acoustic/vortical wave interaction phenomenon. A detailed description of this high-resolution upwind TVD scheme can be found in Refs. 11 and 15. The extension of this scheme to a dynamic grid system, however, is illustrated in the following.

Governing Equations

The unsteady, two-dimensional inviscid Euler flow in a domain V bounded by a boundary S can be expressed in an integral conservation form,

$$\frac{\partial}{\partial t} \int_V U \, dV + \oint_S \boldsymbol{n} \cdot \boldsymbol{F} \, dS = 0 \qquad (1)$$

*Professor, Institute of Aeronautics and Astronautics. Member AIAA.
†Associate Professor, Institute of Aeronautics and Astronautics. Member AIAA.
‡Graduate Research Assistant, Institute of Aeronautics and Astronautics.

In the previous equation the set of conservative variables U and the normal flux vector $F_n = \mathbf{n} \cdot \mathbf{F}$ are given, respectively, by the column vectors:

$$U = \begin{bmatrix} \rho \\ \rho u \\ \rho v \\ \rho e \end{bmatrix}, \qquad F_n = \begin{bmatrix} \rho(u_n - v_n) \\ \rho u(u_n - v_n) + p n_x \\ \rho v(u_n - v_n) + p n_y \\ \rho e(u_n - v_n) + p u_n \end{bmatrix} \qquad (2)$$

where $u_n = \mathbf{u} \cdot \mathbf{n}$ is the normal velocity component, and $v_n = \mathbf{v}_g \cdot \mathbf{n}$ is the normal grid velocity component with n_x and n_y defined as the projections of the unit normal $\mathbf{n}$ in the x and y directions. The variables p, ρ, u, v, and e denote the pressure, density, Cartesian velocity components, and specific total energy, respectively. In closing the previous governing equations, the thermodynamic state equation of a perfect gas is required,

$$p = (\gamma - 1)\left(\rho e - \frac{\rho}{2}\mathbf{u} \cdot \mathbf{u}\right) \qquad (3)$$

in which the specific heat ratio is given by $\gamma = 1.4$.

Applying finite volume discretization, one can approximate the flux terms by the use of an upwind flux-difference scheme[14] to result in a semidiscretized system of ordinary differential equations. This system of ordinary differential equations is then integrated using the explicit three-stage Runge–Kutta time-stepping method.[16]

Osher–Chakravarthy Upwind TVD Scheme

The spatial accuracy of this finite volume discretization depends on the construction of the numerical flux function specified at the cell interface. In this study, the Osher–Chakravarthy MUSCL type upwind scheme[14] based on the Roe splitting[17] is employed. Modification has been made on the interpolation of cell interface values to improve the accuracy of the scheme.

At each i-direction cell interface $i + \frac{1}{2}$, let $U^+_{i+\frac{1}{2}}$ and $U^-_{i+\frac{1}{2}}$ denote the values of the conservative variables specified at the right and left sides of the cell interface. This modified MUSCL type upwind TVD scheme, which considers the grid nonuniformity effect, takes the following form[15]:

$$U^-_{i+\frac{1}{2}} = U_i + \chi_i \sum_m \left[(\zeta_i + 2\phi\sigma_i)\tilde{\alpha}^m_{i+\frac{1}{2}} + \frac{1}{\zeta_i}(1 - 2\phi\sigma_i)\tilde{\tilde{\alpha}}^m_{i-\frac{1}{2}} \right] r^m_i$$

$$U^+_{i-\frac{1}{2}} = U_i - \chi_i \sum_m \left[(\zeta_i - 2\phi\sigma_i)\tilde{\alpha}^m_{i+\frac{1}{2}} + \frac{1}{\zeta_i}(1 + 2\phi\sigma_i)\tilde{\tilde{\alpha}}^m_{i-\frac{1}{2}} \right] r^m_i$$

$$(4)$$

in which $\alpha^m_{i\pm\frac{1}{2}}$ are the characteristic variable differences, r^m_i is the mth right eigenvector associated with the mth eigenvalue of the flux Jacobian matrix, and

$$\zeta_i = (s_i + s_{i-1})/(s_i + s_{i+1})$$
$$\chi_i = s_i/(s_{i+1} + 2s_i + s_{i-1}) \qquad (5)$$
$$\sigma_i = s_i/(s_i + s_{i+1})$$

where the geometry-related parameters ζ_i, χ_i, and σ_i are functions of the mean cell width s_i (defined as the distance connecting the centers of the two opposite cell boundaries) in the i direction.

The monotonicity property of the TVD scheme is guaranteed using the slope limiter given by

$$\tilde{\alpha}^m_{i+\frac{1}{2}} = \text{minmod}\left(\alpha^m_{i+\frac{1}{2}}, \beta\alpha^m_{i-\frac{1}{2}}\right)$$
$$\tilde{\tilde{\alpha}}^m_{i-\frac{1}{2}} = \text{minmod}\left(\alpha^m_{i-\frac{1}{2}}, \beta\alpha^m_{i+\frac{1}{2}}\right) \qquad (6)$$

In the previous equations, the compression parameter β is defined by[11]

$$\beta = \zeta_i[1 - \chi_i(\zeta_i + 2\phi\sigma_i)]/[\chi_i(1 - 2\phi\sigma_i)] \qquad (7)$$

The magnitude of acoustic disturbance is usually so small that it is very easy to be contaminated. It has been shown[15] that the improved interpolation, Eq. (4), is meaningful for a time-accurate acoustic computation.

Boundary Conditions and the Sound Source Modeling

Sound waves emitted from an airfoil surface can be conceived as resulting from a fluctuating volume flux whose strength either is known (fluid pulsation type) or can be derived equivalently from the membrane motion (structural vibration type). In other words, the sound source pertaining to the present problem is of the "monopole" type as classified in the context of acoustics.

For a cell-centered finite volume method, the physical boundary condition specified on surface with or without blowing or suction usually does not involve directly the static pressure. Static pressure required by the numerical method ought to be derived using momentum equations subject to the given nonpermeable or specified normal flux conditions:

$$(\mathbf{u} - \mathbf{v}_g) \cdot \mathbf{n} = \begin{cases} 0 & \text{for solid wall} \\ v_w & \text{for wall with blowing or suction} \end{cases} \qquad (8)$$

in which v_w is the imposed surface normal velocity that characterizes the sound strength. The density of the issued volume flux can be extrapolated from the adjacent interior cell-averaged values. The determination of the surface pressure, however, must invoke the momentum equations that, as expressed in the computational domain (ξ, η, τ), take the form[11]

$$\sqrt{\eta_x^2 + \eta_y^2}\frac{\partial p}{\partial n} = \rho\left[\frac{\partial}{\partial\tau}\eta_t + u\frac{\partial}{\partial\tau}\eta_x + v\frac{\partial}{\partial\tau}\eta_y\right.$$
$$\left. - \bar{U}\left(\eta_x\frac{\partial u}{\partial\xi} + \eta_y\frac{\partial v}{\partial\xi}\right) - \Pi_w\right] \quad \text{for solid wall} \qquad (9a)$$

$$\Pi_w = \begin{cases} 0, \\ \frac{\partial}{\partial\tau}\bar{V}_w + \bar{V}_w\left(\frac{\partial u}{\partial\eta}\eta_x + \frac{\partial v}{\partial\eta}\eta_y\right) & \text{for wall with} \\ & \text{blowing or suction} \end{cases} \qquad (9b)$$

where $\bar{U}$ [$= (\mathbf{u} - \mathbf{v}_g) \cdot \nabla\xi$] is the ξ-contravariant velocity, and $\bar{V}_w(= v_w\sqrt{\eta_x^2 + \eta_y^2})$ is the given surface volume flux. With all of the terms in Eqs. (9a) and (9b) being properly treated and differenced, $\partial p/\partial n$ can be calculated readily, and the wall pressure can thus be extrapolated using this gradient value and the adjacent cell-centered quantity.

In the far field, the outgoing acoustic wave asymptotically approaches a planar one-dimensional wave that enables the use of the nonreflecting boundary conditions based upon the Riemann invariants in the direction normal to the outer boundary. The tangential velocity component and the entropy can be determined using either the freestream values or those extrapolated from the interior, depending upon the direction of propagation of the corresponding characteristic wave.

Geometric Conservation Law

In the aeroelastic computation, the grid system must be adapted to account for the body deformation and/or the vibrational motion. Care must therefore be exercised in the determination of the cell boundary velocity since the computation of the fluxes across the boundary would be affected by this boundary movement. An incorrect calculation of the cell boundary speed will introduce a spurious mass into or out of the computational domain, leading to nonphysical solutions. Thus, to avoid errors induced by the mesh movement, a geometric conservation law[18] needs to be incorporated in addition to the basic physical conservation laws used.

The geometric conservation law states

$$A(t_2) - A(t_1) = \int_{t_1}^{t_2} \oint \mathbf{n} \cdot \mathbf{v}_g \, dL \, dt \qquad (10)$$

where $[A(t_2) - A(t_1)]$ represents the cell area alteration during the time interval $\Delta t = t_2 - t_1$ and dL is the differential arc length
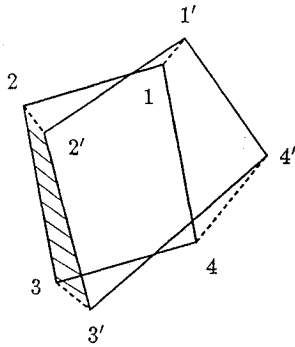
Fig. 1   Schematic of a dynamic cell moving from an old (unprimed) to a new (primed) position.

along the cell boundary. Another constraint condition accompanying Eq. (10) is

$$\oint n \, dL = 0 \tag{11}$$

where n is the unit normal on the cell interface.

Equation (10) defines the relationship between the area change rate with respect to the boundary-edge velocity v_g, whereas Eq. (11) simply states that, at any instant, the finite cell must be closed. Equation (11) often is trivially satisfied since the old and new grid coordinates are known before the calculation of the fluxes. In the present study, the grid nodal coordinates and hence the cell areas $A(t_2)$ and $A(t_1)$ are known, but the appropriate normal cell boundary speeds $v_g \cdot n$ at the cell faces are not explicitly given. Batina adopted a different approach,[19] which assumes that $A(t_2)$ is unknown instead of the grid velocity v_g. Although the geometric conservation law is obeyed, errors committed in the evaluation of the cell area will be accumulated after a long time marching. The present approach avoids this drawback by choosing appropriate cell boundary speeds $v_g \cdot n$ and lets the geometric conservation law be strictly satisfied on each finite volume at any instant.[20,21]

The averaged normal speed associated with each side of the control volume can be obtained by applying Eq. (10) to the line segment of interest:

$$\Delta A_k = \int_{t_1}^{t_2} \int_{L(t)_k} n \cdot v_g \, dL \, dt, \qquad k = 1, 2, 3, 4 \tag{12}$$

Figure 1 shows a sketch of this deformed dynamic cell. Taking the side $\overline{23}$ as an example, the area increment (the hatched area) swept by the movement of the cell side $\overline{23}$ can be evaluated using the given initial and final nodal coordinates. Then the time-averaged normal grid velocity of this cell boundary can be obtained using Eq. (12):

$$(\widetilde{v_g \cdot n}) \equiv \tilde{v}_n = \frac{\Delta A}{\tilde{L} \Delta t} \tag{13}$$

Note that there exists a certain arbitrariness in defining the cell boundary length $\tilde{L}$. For an explicit scheme, $\tilde{L} = L^{(n)}$, and otherwise $\tilde{L} = L^{(n+1)}$ for an implicit scheme. Since the present scheme is an explicit three-stage Runge–Kutta method, the evaluation of $\tilde{L}$ at each stage is defined using $\tilde{L} = L^{(n)}$.

Since the geometric conservation law is equivalent to the physical conservation equations applied on a uniform parallel stream, the grid normal velocity so determined, i.e., Eq. (13), must be consistent with the physical conservation law when marched over a uniform stream using the designed time-stepping algorithm. This consistency requirement is satisfied for the present Runge–Kutta stepping by noting that the kth stage may be viewed as an Euler explicit marching of the variable $W^{(k)}$ from $W^{(0)}$ in a time interval $\alpha_k \Delta t$. The nodal coordinates of the cell at the kth stage, however, are defined by linearly weighting between the old and the new coordinates at time level (n) and $(n + 1)$ using the parameter α_k.

As the geometrical conservation law is marched in conjunction with the physical conservation law by the Runge–Kutta method,

the calculation of the residuals at the k stage is actually performed according to

$$U^{(k)} A^{(k)} = U^{(0)} A^{(0)} - \alpha_k \Delta t R\left[U^{(k-1)}; \ \tilde{v}_n^{(k)}, \ n^{(n)}\right]$$

$$\tilde{v}_n^{(k)} = \frac{\Delta A^{(k)}}{\alpha_k L^{(n)} \Delta t} \tag{14}$$

where the grid system at time level (n) is taken in defining the finite volume while evaluating the residual. It is easy to see that Eq. (14) recovers the geometric conservation law when applied on a uniform stream with constant flow properties.

Aeroelastic Time Marching

A typical section model (see Fig. 2) consisting of plunging and pitching modes is considered. The governing equations of this aeroelastic system read

$$m\frac{d^2\bar{h}}{dt^2} + S_\alpha \frac{d^2\alpha}{dt^2} + K_h \bar{h} = Q_h$$

$$S_\alpha \frac{d^2\bar{h}}{dt^2} + I_\alpha \frac{d^2\alpha}{dt^2} + K_\alpha \alpha = Q_\alpha \tag{15}$$

in which $\bar{h}$ and α are the plunging and pitching displacements; m, S_α, and I_α are the mass, static mass moment, and mass moment of inertia of the typical section (per unit span), respectively; K_h and K_α are the spring constants for plunging and pitching motions, and Q_h and Q_α are the generalized aerodynamic forces for plunging and pitching modes. In this model problem, no structural damping is included; therefore, the damping of this dynamic system, positive or negative, comes entirely from the aerodynamic contribution. Sound waves are emitted from a slot near the trailing edge (see Fig. 2), with the strength assumed given. In practice, a pure two-dimensional acoustic field is hard to generate. Discussions on the three dimensionality of the present acoustic excitation technique deserve close attention in future studies.

The governing equations, as appropriately nondimensionalized, can be put in a discrete time-marching matrix equation form expressed by states at steps (n) and $(n-1)$:[22]

$$X^{n+1} = \phi(T)X^n + \theta B(3\bar{u}^n - \bar{u}^{n-1})/2 \tag{16}$$

in which $\phi(T) = \exp[AT]$ is the state transition matrix,

$$\theta = \int_0^T \phi(T - \tau) \, d\tau \tag{17}$$

$$X = \begin{bmatrix} h \\ \alpha \\ h' \\ \alpha' \end{bmatrix}, \qquad A = \begin{bmatrix} 0 & I \\ M^{-1}K & 0 \end{bmatrix}, \qquad B = \begin{bmatrix} 0 \\ M^{-1}\bar{B} \end{bmatrix} \tag{18}$$
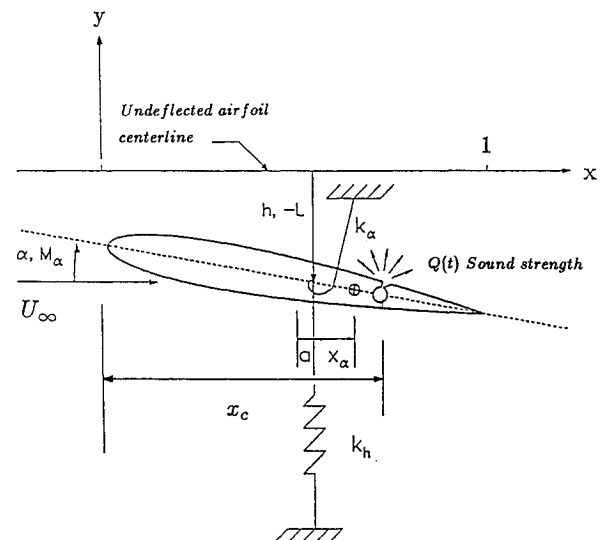

Fig. 2   Schematic of typical section model with acoustic excitation.

and

$$\bar{u} = \left\{ \begin{matrix} C_L \\ C_M \end{matrix} \right\}, \qquad \bar{B} = \frac{2}{\pi \mu} \begin{bmatrix} -1 & 0 \\ 0 & 1 \end{bmatrix} \qquad (19)$$

In the previous equations, $h \equiv \bar{h}/b$ where b is the half-chord, M and K are the mass and stiffness matrices, C_L and C_M are the aerodynamic lift and pitching moment coefficients, the superscript ' denotes the dimensionless time derivative (nondimensionalized by $1/\omega_\alpha$), and μ is the mass ratio. The matrices ϕ, θ, and B are not functions of time and can be calculated analytically and stored for the subsequent use.

The marching step size T is usually constrained by the Courant–Friedrichs–Lewy (CFL) number associated with the aerodynamic flow solver. The requirement of a time-accurate shock-capturing[23] poses another limitation on the time-marching size, namely, the stepping size T should be so chosen that the shock wave will move no more than one cell during a single time stepping.

Grid Update

The unsteady aerodynamic loads generated in the present aeroelastic system are known resulting from the airfoil surface movement caused by either a rigid-body motion or a structural deformation. The grid system, hence, should be updated according to the calculated states h, α, h', and α'. The present grid adaptation modifies Batina's approach,[19] in which the inner grid boundary moves with the airfoil surface, whereas the outer boundary is kept stationary. Batina designed a predictor/corrector procedure to determine the new grid positions. In the predictor stage, we replaced Batina's scheme by that of Huff.[24] The grid displacements estimated in the predictor stage are determined using a weighting function method with weighting gradually reduced from the inner boundary to the outer far-field boundary. Then a corrector procedure is enforced to iteratively smooth and redistribute the grid coordinates via a spring network analogy. In general, the smoothness of the new grid is dependent on the iteration number of the corrector. It was found in the present study that five iterations are in general sufficient for the present test cases and the time-stepping size selected. It was also found that insufficient iterations of the corrector scheme may lead to erroneous time responses that often are difficult to discern and may obscure the physical explanations.

III. Aeroelastic Code Validation

At the present time, there exist no acoustic flutter suppression experiments that have been performed in the transonic region. A direct validation of the code is therefore impossible. However, indirect checks can be carried out to examine the various aspects of the code. It is believed that as the scheme is subjected to these tests, the subsequent transonic acoustic flutter suppression study will be more convincing and thus pave the way for future investigations.

This validation consists of a forced pitching oscillation, an open-loop flutter imulation, and an incompressible acoustic flutter suppression previously studied analytically.

Forced Pitching Oscillation

A NACA 0012 airfoil (C-type grid, 96 × 16 cells) is forced to pitch about a pivot point at the quarter-chord position. The freestream Mach number is $M_\infty = 0.755$, and the pitching motion is governed by

$$\alpha(t) = \alpha_m + \alpha_0 \sin kt, \qquad (20)$$

with $\alpha_m = 0.016$ deg, $\alpha_0 = 2.51$ deg, and the reduced frequency $k = \omega c/U_\infty = 0.1628$. The experimental results are well documented[25] so that comparisons can be made to check the scheme's accuracy. This test does not involve the structural equation; hence, the aerodynamic part can be examined independently. The major elements of the solver that can be checked are the shock-capturing capability, the dynamic grid system, and the geometric conservation law implementation. The instantaneous pressure distributions at several instants during this pitching oscillation are illustrated in Fig. 3, in which the excursion, emergence, and disappearance of the shock wave are seen to be sufficiently resolved.
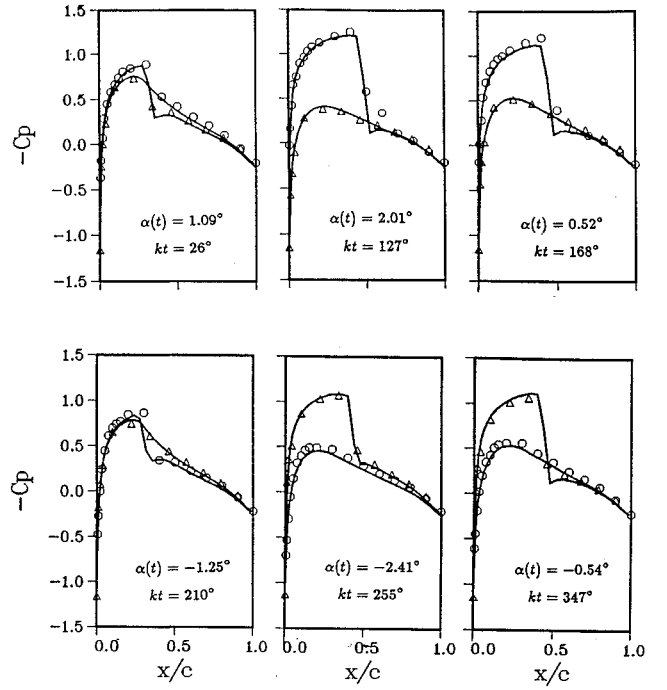

Fig. 3 Comparisons of instantaneous pressure distributions for the NACA 0012 airfoil pitching at $M_\infty = 0.755$, $\alpha(t) = \alpha_m + \alpha_0 \sin kt$, $\alpha_m = 0.016$ deg, $\alpha_0 = 2.51$ deg, and $k = 0.1628$ (solid line: present numerical solution, and open mark: experiment).
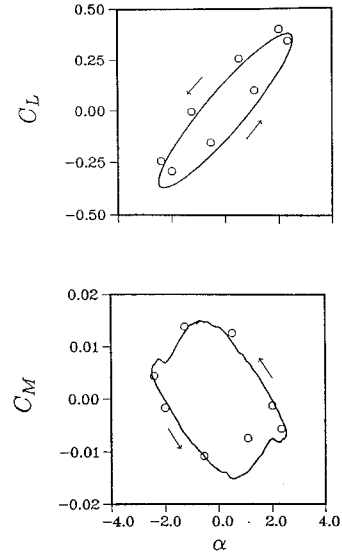

Fig. 4 Comparisons of lift and pitching moment coefficients vs instantaneous angle of attack for the NACA 0012 airfoil pitching at $M_\infty = 0.755$, $\alpha(t) = \alpha_m + \alpha_0 \sin kt$, $\alpha_m = 0.016$ deg, $\alpha_0 = 2.51$ deg, and $k = 0.1628$ (solid line: present numerical solution, open mark: experiment, and arrow sign indicates the direction of increasing time).

The computed lift and pitching moment coefficients against angle of attack are depicted in Fig. 4. The agreement in data achieved in the C_L and C_M plots is seen to be satisfactory.

Transonic Flutter Test

The additional aspect added relative to the preceding forced oscillation simulation is the coupling of the structure and the fluid time integrators. The transonic flutter case tested has a steady-state condition for $M_\infty = 0.85$ and $\alpha_m = 0$ deg. A NACA 64A006 airfoil shape was selected, and the structural parameters were given by $a_h = -0.50$, $x_\alpha = 0.25$, $r_\alpha = 0.50$, $\omega_h/\omega_\alpha = 0.20$, and $\mu = 95$.
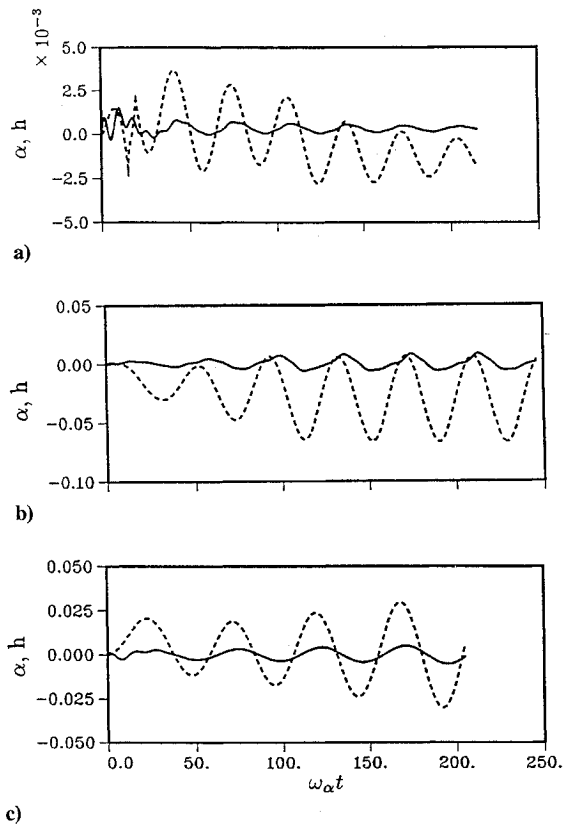
Fig. 5   Effect of reduced velocity on the responses of the NACA 64A006 airfoil at M_∞ = 0.85, α_m = 0.0 deg, a_h = −0.5, x_α = 0.25, r_α = 0.50, ω_h/ω_α = 0.2, and μ = 95; a) V^* = 3.0, b) V^* = 4.75, and c) V^* = 5.4 (solid line: pitching mode, and dash line: plunging mode).
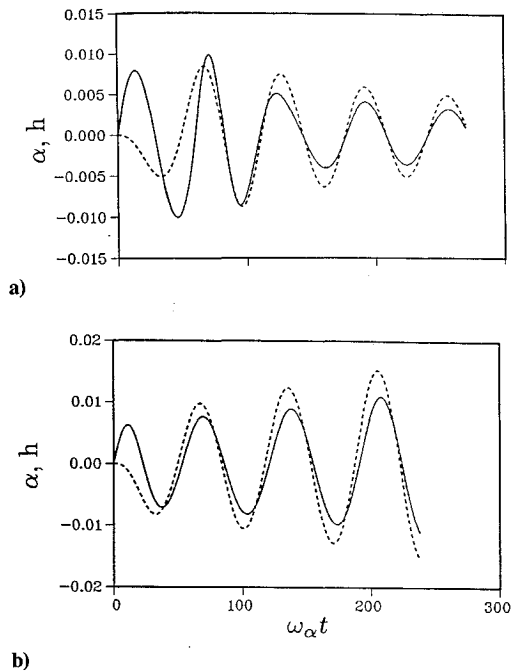

Fig. 6   Effect of reduced velocity on the closed-loop responses of the NACA 64A006 airfoil at M_∞ = 0.2, α_m = 0.0 deg, a_h = −0.4, x_α = 0.2, r_α = 0.50, ω_h/ω_α = 0.5, μ = 40, and G_α = −0.25; a) V^* = 3.5 and b) V^* = 4.5 (solid line: pitching mode, and dash line: plunging mode).

There were three reduced velocities $V^*(\equiv V/b\omega_a)$ = 3.0, 4.75, and 5.4 that were selected for the present time-domain analysis. Initiation of the motion was done by a four-cycle pitching motion with an amplitude of 1 deg and a reduced frequency 1.50. Figure 5 shows the responses pertaining, respectively, to the subcritical (stable), nearly neutral, and supercritical (unstable) categories. The damping and frequency of the responses can be estimated using the model identification technique[26]:

$$X_i(t) = a_{i,0} + \sum_{j=1}^{m} e^{\sigma_j t}[a_{i,j}\cos(\omega_j t) + b_{i,j}\sin(\omega_j t)]$$

$$i = 1, \, m \qquad (21)$$

where m is the number of modes. Flutter velocity and frequency are defined when the largest damping ratio vanishes, $\sigma_i = 0$.

In the present simulation the flutter reduced velocity and frequency calculated are 4.734 and 0.148, whereas 4.7 and 0.15 were obtained by Guruswamy and Yang [27] in which the LTRAN2 potential code was employed.

Acoustic Flutter Suppression in Incompressible Flow

All of the tests conducted in the preceding subsections were of the open-loop type, but the integration involving the dynamic grid system, acoustic excitation, and the combined structure/fluid/acoustic time-marching algorithm were not examined. Since no experiments are available for comparison, we choose to compare our numerical procedure (time-domain analysis) with results obtained analytically using V-g (frequency-domain analysis) and root-locus (S-domain analysis) methods. The analytic methods were developed for the incompressible flow; therefore, as the present compressible Euler code is used, the compressibility effect of the flow is minimized using a low Mach number M_∞ = 0.2, which allows for an affordable step size during the time marching.

The structural parameters defined for this acoustic flutter suppression case are a_h = −0.4, x_α = 0.2, r_α = 0.5, ω_h/ω_α = 0.5,

and μ = 40. The sound source is located around the airfoil trailing edge, x_c = 0.98, and is activated according to the feedback control law

$$Q(t) = -0.25\alpha(t) \qquad (22)$$

where $Q(t)$ is the sound source strength, and $\alpha(t)$ is the instantaneous pitching angle. The analytic results predicted by the V-g method were a flutter speed V_F^* = 3.5932 and a flutter frequency ω_F/ω_α = 0.7698, whereas V_F^* = 3.5162 and ω_F/ω_α = 0.7665 were the results obtained by the root-locus method.[10] The time responses calculated using the presently developed acoustic flutter suppression code are presented in Fig. 6. Applying the model identification procedure on these time response histories, the flutter boundary and frequency can be deduced, taking, respectively, the values V_F^* = 3.9 and ω_F/ω_α = 0.7826.

Flow compressibility could be one of the reasons that causes this slight inconsistency. Another reason is attributed to the numerical modeling of the sound source. The induced circulatory airloads are dependent on the acoustic perturbation amplitude at the trailing edge. As the sound source is placed very close to the trailing edge, the distributed type numerical source modeling will differ to a significant extent from that of the theoretical analysis that treats the sound source as a point singularity.

The agreements achieved give us confidence that the present numerical acoustic flutter code is correct, as many individually verified elements including shock capturing, dynamic grid, aeroelastic time integration, and the sound emission model are put together. This allows us to use the code to further explore transonic flow applications.

IV.   Acoustic Flutter Suppression in Transonic Flow

The suppression of flutter instability in an incompressible flow using sound waves has been analyzed previously.[10] The understanding gained from that study stresses the importance of choosing the correct phase between the motion and the structurally and acoustically generated airloads. The magnitude of the gain or the sound strength employed, however, may affect the damping or the growth rate of the motion. For the present time-domain analysis, the phase lag used previously in the frequency-domain analysis will be transformed into a time delay appearing in the time argument of the feedback control law. For instance, a control law based on the sensed pitching
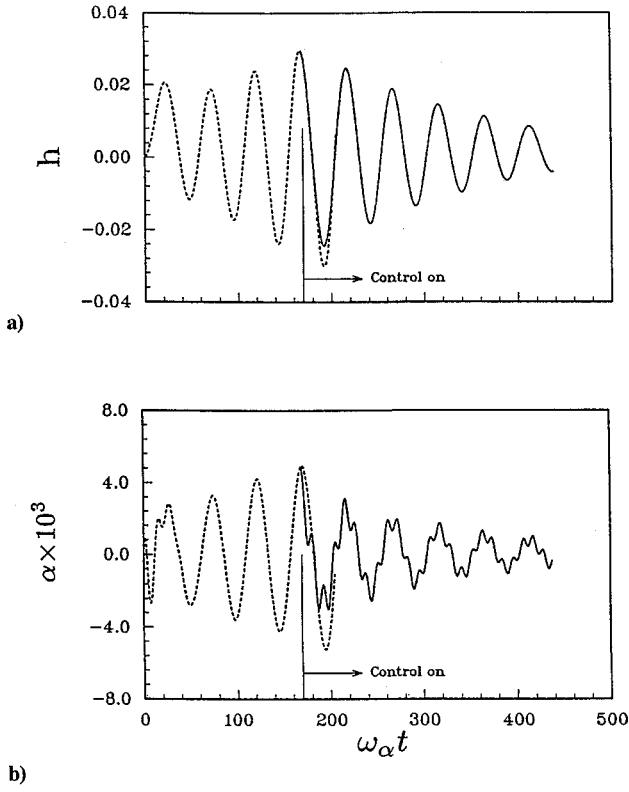
Fig. 7   Transient responses for acoustically suppressed flutter at M_∞ = 0.85, α_m = 0.0 deg, V^* = $1.14V_F^*$, G_α = −0.25, and x_c = 0.92; a) plunging mode and b) pitching mode (solid line: closed-loop solution, and dash line: open-loop solution).
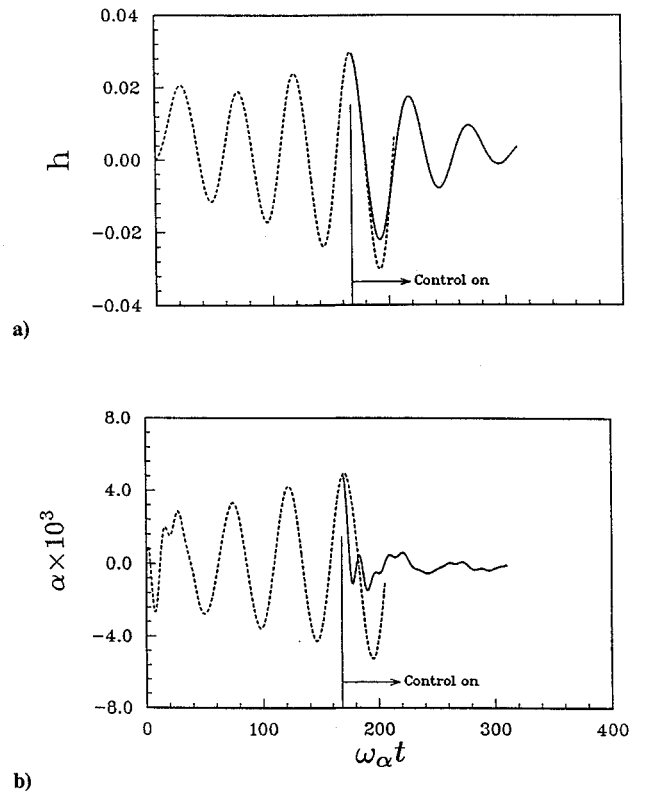

Fig. 9   Transient responses for acoustically suppressed flutter at M_∞ = 0.85, α_m = 0.0 deg, V^* = $1.14V_F^*$, G_h = −0.05, and x_c = 0.92; a) plunging mode and b) pitching mode (solid line: closed-loop solution, and dash line: open-loop solution).
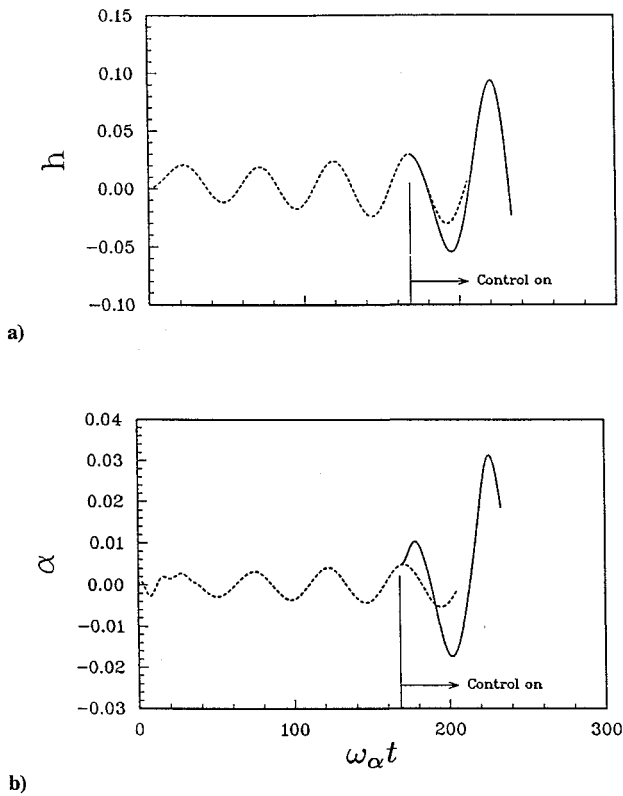

Fig. 8   Transient responses for acoustic excitations at M_∞ = 0.85, α_m = 0.0 deg, V^* = $1.14V_F^*$, G_α = 0.25, and x_c = 0.92; a) plunging mode and b) pitching mode (solid line: closed-loop solution, and dash line: open-loop solution).
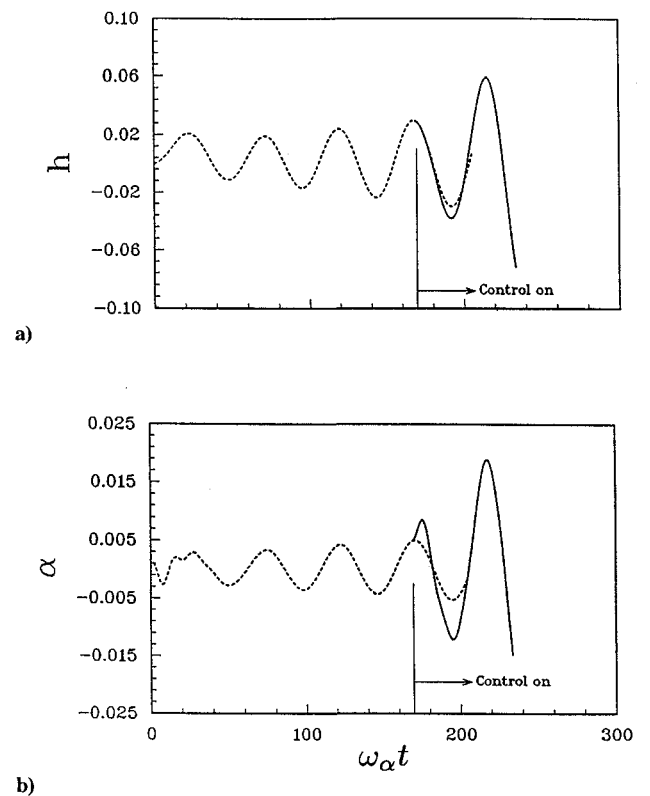

Fig. 10   Transient responses for acoustic excitations at M_∞ = 0.85, α_m = 0.0 deg, V^* = $1.14V_F^*$, G_h = 0.05, and x_c = 0.92; a) plunging mode and b) pitching mode (solid line: closed-loop solution, and dash line: open-loop solution).
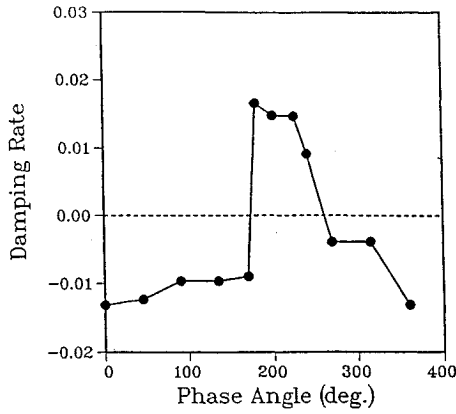
Fig. 11 Damping rate vs phase angle using closed-loop feedback control on NACA 64A006 airfoil; M_∞ = 0.85, α_m = 0.0 deg, V^* = 1.14V_F^*, x_c = 0.92, and G_h = 0.25.
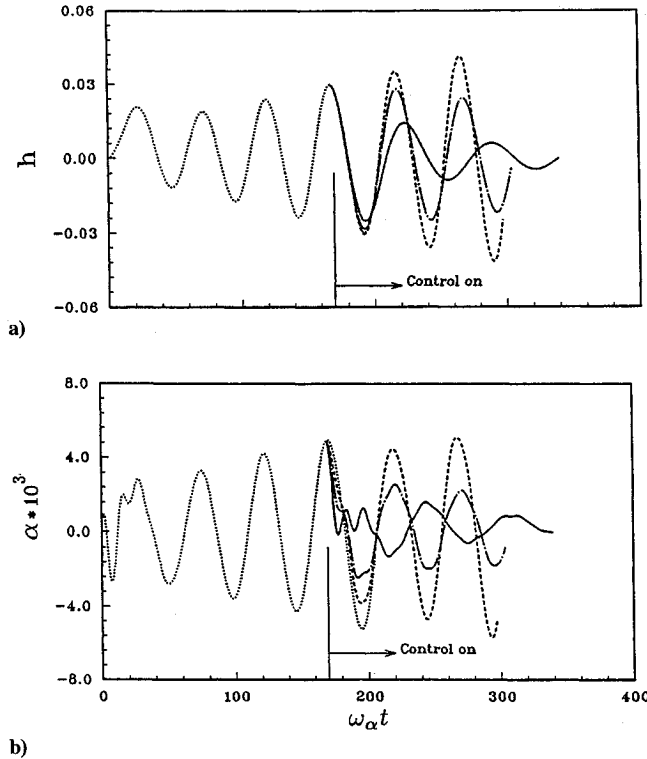

Fig. 12 Transient responses of acoustically controlled flutter motions, NACA 64A006 airfoil, M_∞ = 0.85, α = 0.0 deg, and V^* = 1.14V_F^*; structural parameters: a_h = −0.5, x_α = 0.25, r_α = 0.5, ω_h/ω_α = 0.2, and μ = 95; feedback gain and phase: G_h = 1/20 and ϕ = 225 deg; a) plunging mode and b) pitching mode (· · · · · : open loop, — — —: x_c = 0.77,— · —: x_c = 0.85, and —: x_c = 0.92).

Fig. 13 Transient response and energy supply histories of an acoustically suppressed flutter motion, NACA 64A006 airfoil, M_∞ = 0.85 and α = 0.0 deg; structural parameters: a_h = −0.5, x_α = 0.25, r_α = 0.5, ω_h/ω_α = 0.2, and μ = 95; V^* = 1.14V_F^*; feedback gain and phase: G_h = 1/60 and ϕ = 225 deg; forcing location: x_c = 0.92; a) plunging mode, and b) pitching mode, and c) acoustic energy supplied (dash line: open loop, and solid line: closed loop).

The following parametric studies have been conducted so as to give a clearer understanding of this new flutter control technique.

Phase Angle Effect

To show the gain phase effect on the closed-loop stability, several feedback phase angles were tested, and Fig. 11 shows the simulated results where the forcing location and gain specified were x_c = 0.92 and G_h = 0.05, respectively. It is shown that the feedback phase angle leading to suppressed motion (positive damping ratio) lies between 180 to 260 deg, and the optimal flutter suppression phase angle is around 180 deg. The phenomenon of sign reversal of the damping ratio around 180-deg phase angle is quite unusual and was not seen in the incompressible study.[10] The reason is not clear and deserves further investigation.

Forcing Location Effect

In the investigation of acoustically excited transonic flow, it was found that the forcing location is an important control parameter for determining the shock excursion type. As pointed out in Ref. 11, both direct impingement of acoustic waves and upstream influence of shedding vorticity waves can affect the shock motion. Which of these two mechanisms is more dominant depends on the forcing location. Different excitation locations may result in different shock types and phase lags relative to the forcings. Therefore, it is expected that as the active acoustic excitation technique is applied on a fluttering airfoil, the most suitable phase angle and the damping ratio will change when forcing location varies, as shown in Fig. 12. It is shown in Fig. 12 that the closer the distance between the forcing location and the trailing edge, the more effective the present suppression technique.

angle can be expressed as

$$Q(t) = G_\alpha \cdot \alpha(t - \tau) \tag{23}$$

where G_α is the gain magnitude and τ is the time delay.

The extension of the low-speed acoustic flutter suppression technique to the transonic flow region is inspired by the success of controlling the shock motion via a trailing-edge acoustic forcing.[11] Here we still use the previous NACA 64A006 typical section case (see Figs. 5 and 6) as the model for illustration. Mach number is set to be M_∞ = 0.85, and flutter occurs at V_F^* = 4.734. Successful flutter suppressions of a supercritical case, V^* = 1.14V_F^*, using plunging or pitching as the sensed state are illustrated in Figs. 7–10. The gain magnitudes were so chosen, $|G_\alpha|$ = 0.25 and $|G_h|$ = 0.05, that the sound waves emitted in these cases were of comparable strengths. For the present study, out-of-phase gains are found effective, whereas in-phase gains fail in suppressing the flutter instability.
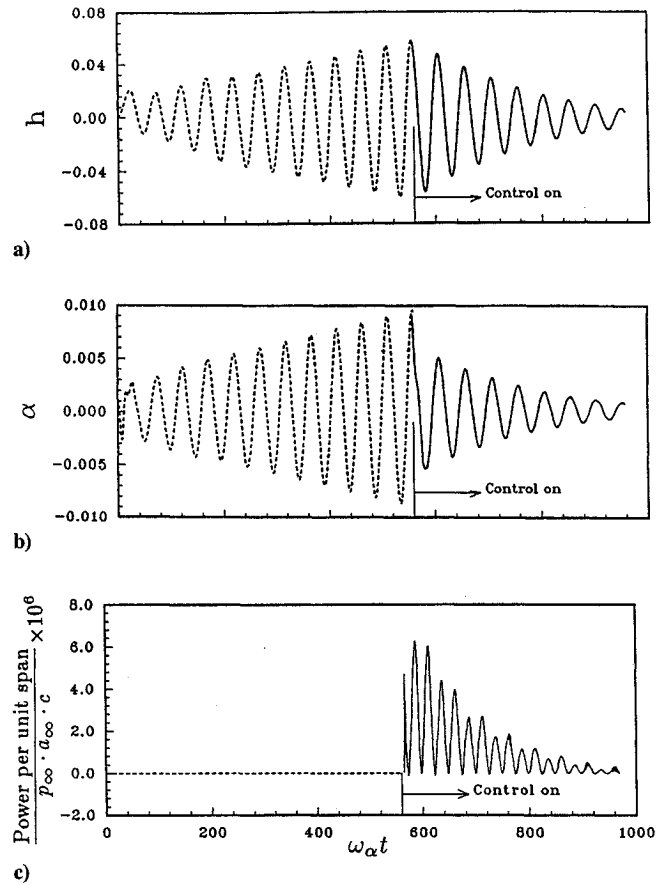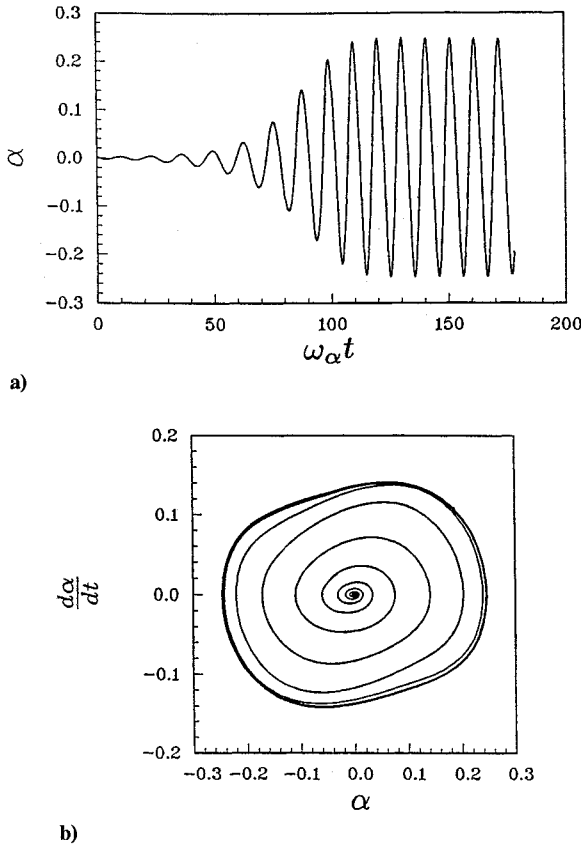
Fig. 14 Limit cycle responses of a NACA 64A006 airfoil, M_∞ = 0.85, α_m = 0.0 deg, a_h = -0.2, x_α = 0.2, r_α^2 = 0.29, ω_h/ω_α = 0.34335, μ = 10, and V^* = 2.25; a) pitching response and b) phase plane portrait of pitching response vs pitching rate.

Acoustic Energy Supply

It would be interesting to know how much energy is required for generating the sound to suppress the flutter motion. Suppose all of the dissipations were neglected so that the energy input into the sound generator has been transformed entirely into the energy content of the acoustic wave radiated away. An energy balance relationship in an acoustic field forced by a monopole can be expressed by[11]

$$\int_V \left(\frac{\partial E}{\partial \tau} + \nabla \cdot I \right) dV = \sum_{i=1}^{3} p_i' Q_i \tag{24}$$

where E and I are the acoustic energy density and acoustic flux vector, respectively. This relationship describes the energy contents among the stored acoustic energy in the volume, $\int_V E \, dV$, the energy flux across the control surface, $\oint_S I \cdot n \, dS$, and the energy supplied from a monopole source located on the wall, $\sum_i p_i' Q_i$.

A suppressed flutter test is conducted, and Eq. (24) is used to obtain the power consumption required to suppress the originally unstable system. Figure 13 shows the results of this selected problem: M_∞ = 0.85, α_m = 0.0 deg, a_h = -0.5, x_α = 0.25, r_α = 0.5, ω_h/ω_α = 0.2, μ = 95, and the feedback gain and phase, G_h = 1/60 and ϕ = 225 deg, with the plunging mode displacement used as the feedback state. Presented in Fig. 13c is the time history of the dimensionless acoustic energy supplied. The maximum level amounts to about 100 W per unit span (meter) if a flight altitude of 10,000 m and a chord length of 3 m are assumed. This acoustic energy level can be reduced futher provided an optimal feedback control logic is sought.

Limitation of the Acoustic Excitation Technique

It was reported in the original experimental work[9] that this acoustic flutter suppression is only applicable for flutter motions with small amplitudes. The underlying reason was not clear, nor can it be answered with the linear analysis since vibrational magnitude is not
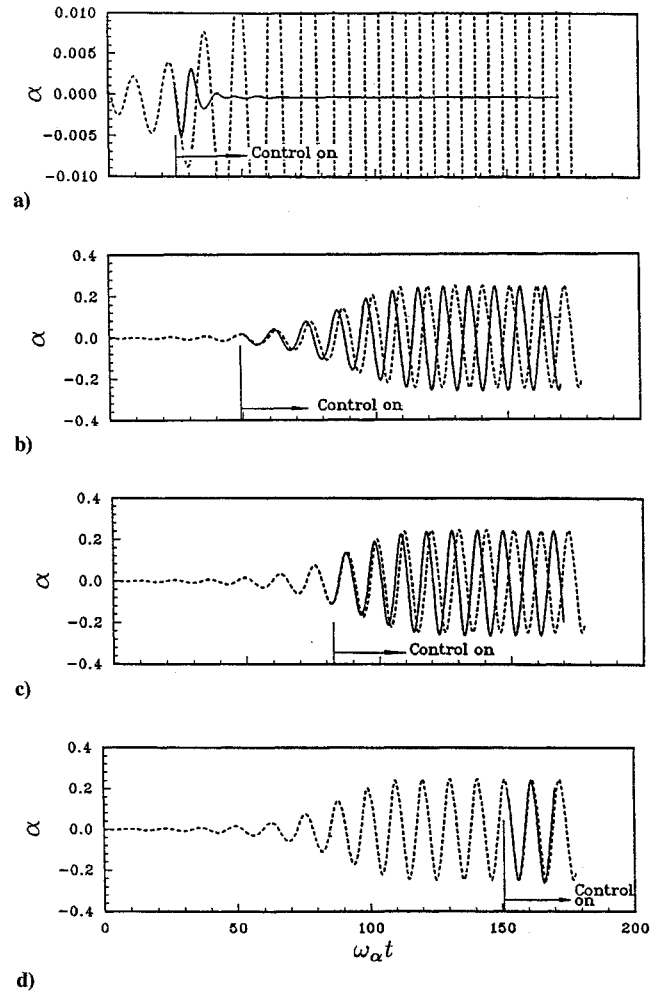

Fig. 15 Pitching responses of acoustic feedback control initiated at several instants of a limit cycle motion, M_∞ = 0.85, α_m = 0.0 deg, a_h = -0.2, x_α = 0.2, r_α^2 = 0.29, ω_h/ω_α = 0.34335, μ = 10, V^* = 2.25, and G_α = -0.025, control initiated at time a) t = 25, b) t = 50, c) t = 81, and d) t = 151.

a parameter that can affect the stability characteristics of the linear system.

Limit cycle oscillation is a frequently observed phenomenon in the transonic flutter problem. Its amplitude is often large, and it is interesting to see whether the present acoustic technique can cope with this limit cycle type large-amplitude oscillation. A limit cycle oscillation was first generated (see Fig. 14) using the present NACA 64A006 model, with parameters a_h = -0.2, x_α = 0.2, r_α^2 = 0.29, ω_h/ω_α = 0.34335, μ = 10.0, and V^* = 2.25.[28] The pitching amplitude reaches a high value of α = 0.24 ($\simeq$14 deg). There are four instants that have been tested to initiate the active acoustic control device. One is at the early infinitesimal stage t = 25 (the maximum pitching angle $\alpha \simeq$ 5.3 × $10^{-3} \simeq$ 0.303 deg); two are situated in the transient stage toward the full limit cycle, t = 50 ($\alpha \simeq$ 0.0168 $\simeq$ 0.963 deg) and t = 81 ($\alpha \simeq$ $-0.1097 \simeq$ -6.285 deg); and the last is selected when the limit cycle is saturated, t = 151 ($\alpha \simeq$ 0.1843 $\simeq$ 10.560 deg). The results are presented in Fig. 15. Except for the smallest α case, all of the remaining acoustic excitation experiments show an inability to suppress the large-amplitude oscillation. This illustrates the limitation of the present acoustic flutter suppression technique and points out the need for developing sensitive sensor devices to detect and suppress the oscillations as early as possible.

V. Concluding Remarks

A preliminary study of acoustic flutter suppression using a transonic Euler flow has been conducted. The Osher–Chakravarthy upwind TVD scheme with modifications made on the reconstruction

of the interface variables has been incorporated successfully on a dynamic mesh system. To avoid nonphysical mass flux produced due to grid motion, the geometric conservation law was used in conjunction with the physical conservation laws. Consistency in the time marching of the geometric and the physical conservation laws was achieved by a properly defined cell boundary speed.

This aeroelastic time-domain solver was first validated through a series of tests including forced pitching oscillation, open-loop transonic flutter, and closed-loop active acoustic flutter suppression in an incompressible flow. Sufficient confidence has been gained that indicates that the present structure/fluid/acoustic solver is reliable and hence can be used to perform transonic flutter suppression studies.

From the simulation results obtained, it was shown that transonic flutter can be suppressed using an appropriately controlled sound generator. As was found in the previous incompressible flow investigations, the important control parameters are the phase and the amplitude of the control gain. Moreover, the forcing location is also very influential, in particular when the sound generator is placed near the airfoil trailing edge. Finally, a limit cycle type large-amplitude oscillation was investigated to see whether a large-amplitude oscillation can be damped using the present technique. The results show that the acoustic suppression can only be effective for suppressing small oscillations. This conclusion is consistent with previous wind-tunnel test results.

The general recommendations drawn from this numerical investigation are that acoustic flutter suppression in the transonic flow is feasible; however, care must be exercised to use sensor devices that can detect and suppress the oscillations when the perturbations are still small.

References

[1] Ffowcs Williams, J. E., "Anti-Sound," *Proceedings of the Royal Society of London,* Series A, Vol. 395, Sept. 1984, pp. 63–88.

[2] Ffowcs Williams, J. E., "The Aerodynamic Potential of Anti-Sound," *Proceedings of the 15th Congress of the International Council of the Aeronautical Sciences,* (London), Vol. 1, Sept. 1986, pp. 1–13.

[3] Hsiao, F.-B., Liu, C.-F., and Shyu, J.-Y., "Control of Wall-Separated Flow by Internal Acoustic Excitation," *AIAA Journal,* Vol. 28, No. 8, 1990, pp. 1440–1446.

[4] Gad-el-Hak, M., and Bushnell, D. M., "Separation Control: Review," *Transactions of ASME, Journal of Fluids Engineering,* Vol. 113, No. 1, March 1991, pp. 5–30.

[5] Ho, C.-M., and Huerre, P., "Perturbed Free Shear Layers," *Annual Review of Fluid Mechanics,* Vol. 16, 1984, pp. 365–424.

[6] Culick, F. E. C., "Some Recent Results for Nonlinear Acoustics in Combustion Chambers," AIAA Paper 90-3927, Oct. 1990.

[7] Epstein, A. H., Ffowcs Williams, J. E., and Greitzer, E. M., "Active Suppression of Compressor Instabilities," AIAA Paper 86-1914, July 1986.

[8] Moore, F. K., "Theory of Multistage Compressors, Parts 1, 2, and 3," *Transactions of ASME, Journal of Engineering for Power,* Vol. 106, April 1984, pp. 313–336.

[9] Huang, X.-Y., "Active Control of Aerofoil Flutter," *AIAA Journal,*

[10] Vol. 25, No. 8, 1987, pp. 1126–1132.

[10] Lu, P.-J., and Huang, L.-J., "Flutter Suppression of Thin Airfoils Using Active Acoustic Excitations," *AIAA Journal,* Vol. 30, No. 12, 1992, pp. 2873–2881.

[11] Yeh, D.-Y., "Unsteady Aerodynamic and Aeroelastic Behaviors of Acoustically Excited Transonic Flow," Ph.D. Dissertation, Inst. of Aeronautics and Astronautics, National Cheng Kung Univ., Tainan, Taiwan, ROC, 1992.

[12] Ashley, H., "Role of Shock in the 'Sub-Transonic' Flutter Phenomenon," *Journal of Aircraft,* Vol. 17, No. 3, 1980, pp. 187–197.

[13] Bendiksen, O. O., "Role of Shock Dynamics in Transonic Flutter," AIAA Paper 92-2121, 1992.

[14] Chakravarthy, S. R., and Osher, S., "A New Class of High Accuracy TVD Schemes for Hyperbolic Conservation Laws," AIAA Paper 85-0363, Jan. 1985.

[15] Lu, P.-J., Pan, D., and Yeh, D.-Y., "On the Numerical Simulation of Trailing Edge Acoustic/Vortical Interaction," *AIAA Journal,* Vol. 33, No. 8, 1995.

[16] Venkatakrishnan, V., and Jameson, A., "Computation of Unsteady Transonic Flows by the Solution of Euler Equations," *AIAA Journal,* Vol. 26, No. 8, 1988, pp. 974–981.

[17] Roe, P. L., "Approximate Riemann Solvers, Parameter Vectors, and Difference Schemes," *Journal of Computational Physics,* Vol. 43, 1981, pp. 357–372.

[18] Vinokur, M., "Review Article: An Analysis of Finite-Difference and Finite-Volume Formulations of Conservation Laws," *Journal of Computational Physics,* Vol. 81, 1989, pp. 1–52.

[19] Batina, J. T., "Unsteady Euler Airfoil Solutions Using Unstructured Dynamic Meshes," AIAA Paper 89-0115, Jan. 1989.

[20] Demirdzic, I., and Peric, M., "Space Conservation Law in Finite Volume Calculations of Fluid Flow," *International Journal for Numerical Methods in Fluids,* Vol. 8, 1988, pp. 1037–1050.

[21] Demirdzic, I., and Peric, M., "Finite Volume Method for Prediction of Fluid Flow in Arbitrarily Shaped Domains with Moving Boundaries," *International Journal for Numerical Methods in Fluids,* Vol. 10, 1990, pp. 771–790.

[22] Edwards, J. W., Bennett, R. M., Whitlow, W., Jr., and Seidel, D. A., "Time-Marching Transonic Flutter Solutions Including Angle-of-Attack Effects," *Journal of Aircraft,* Vol. 20, No. 11, 1983, pp. 899–906.

[23] Rizzetta, D. P., "Time-Dependent Response of a Two-Dimensional Airfoil in Transonic Flow," *AIAA Journal,* Vol. 17, No. 1, 1979, pp. 26–32.

[24] Huff, D. L., "Numerical Simulations of Unsteady, Viscous, Transonic Flow over Isolated and Cascaded Airfoils Using a Deforming Grid," AIAA Paper 87-1316, June 1987.

[25] Landon, R. H., "NACA 0012 Oscillating and Transient Pitching," Data Set 3 in AGARD-R-702, *Compendium of Unsteady Aerodynamic Measurements,* Aug. 1982.

[26] Bennett, R. M., and Desmarais, R. N., "Curve Fitting of Aeroelastic Transient Response Data with Exponential Functions," *Flutter Testing Techniques,* NASA SP-415, May 1975, pp. 43–58.

[27] Guruswamy, P., and Yang, T.-Y., "Aeroelastic Time Response Analysis of Thin Airfoils by Transonic Code LTRAN2," *Computers and Fluids,* Vol. 9, No. 4, 1980, pp. 409–425.

[28] Kousen, K. A., "Nonlinear Phenomena in Compressible Transonic Aeroelasticity," Ph.D. Dissertation, Dept. of Mechanical and Aerospace Engineering, Princeton Univ., Princeton, NJ, 1989.